

Tidal flow over topography: effect of excursion number on wave energetics and turbulence

Masoud Jalali, Narsimha R. Rapaka and Sutanu Sarkar[†]

Mechanical and Aerospace Engineering, University of California, San Diego, La Jolla, CA 92093, USA

(Received 30 October 2013; revised 15 March 2014; accepted 5 May 2014;
first published online 9 June 2014)

The excursion number, $Ex = U_0/\Omega l$, is a parameter that characterizes the ratio of streamwise fluid advection during a tidal oscillation of amplitude U_0 and frequency Ω to the streamwise topographic length scale l . Direct numerical simulations are performed to study how internal gravity waves and turbulence change when Ex is varied from a low value (typical of a ridge in the deep ocean) to a value of unity (corresponding to energetic tides over a small topographic feature). An isolated obstacle having a smoothed triangular shape and 20% of the streamwise length at critical slope is considered. With increasing values of Ex , the near field of the internal waves loses its beam-like character, the wave response becomes asymmetric with respect to the ridge centre, and transient lee waves form. Analysis of the baroclinic energy balance shows significant reduction in the radiated wave flux in the cases with higher Ex owing to a substantial rise in advection and baroclinic dissipation as well as a decrease in conversion. Turbulence changes qualitatively with increasing Ex . In the situation with $Ex \sim 0.1$, turbulence is intensified at the near-critical regions of the slope, and is also significant in the internal wave beams above the ridge where there is intensified shear. At $Ex = O(1)$, the transient lee waves overturn adjacent to the ridge flanks and, owing to convective instability, buoyancy acts as a source for turbulent kinetic energy. The size of the turbulent overturns has a non-monotonic dependence on excursion number: the largest overturns, as tall as twice the obstacle height, occur in the $Ex = 0.4$ case, but there is a substantial decrease of overturn size at larger values of Ex simulated here.

Key words: internal waves, stratified turbulence, topographic effects

1. Introduction

Mixing mediates the distribution of heat, salt and oxygen in the ocean and, therefore, its physical and biological state. Internal tides, which are internal gravity waves generated by the interaction of an oscillating barotropic flow of a density-stratified fluid over bottom topography, constitute a major pathway to diapycnal mixing in the deep ocean (Polzin *et al.* 1997; Munk & Wunsch 1998; Ledwell *et al.* 2000; St Laurent, Toole & Schmitt 2001) and, by affecting the ocean stratification and drag on currents, they also play an important role in the large-scale circulation (Simmons *et al.* 2004; Saenko & Merryfield 2005). Intensified turbulent dissipation

[†] Email address for correspondence: ssarkar@ucsd.edu

associated with internal tides can be found near seamounts (Kunze & Toole 1997; Lueck & Mudge 1997), submarine ridges (Rudnick *et al.* 2003; Klymak *et al.* 2006), submarine canyons (Polzin *et al.* 1996; Carter & Gregg 2002; Wain *et al.* 2013) and the continental slope (Cacchione, Pratson & Ogston 2002; Moum *et al.* 2002; Nash *et al.* 2007).

In considering the generation of internal waves by horizontal oscillation of fluid particles over an obstacle in a stratified fluid, several important physical parameters arise in inviscid flow, as discussed by Garrett & Kunze (2007): the barotropic forcing frequency Ω ; the buoyancy frequency N_∞ ; the Coriolis frequency f ; the height h and length l of the topography; the depth H of the ocean; and the amplitude of the barotropic tidal velocity U_0 . Key non-dimensional parameters are as follows. The slope criticality, $\epsilon = \tan \beta / \tan \theta$, measures the steepness of the topography with slope $\tan \beta$ relative to the internal wave characteristic with slope $\tan \theta = \sqrt{(\Omega^2 - f^2)/(N_\infty^2 - \Omega^2)}$. The excursion number, $Ex = U_0/\Omega l$, characterizes the ratio of the background fluid excursion during one tidal cycle to the streamwise length scale of the topography. The height change in topography compared to the depth of the ocean, $h_r = h/H$, determines the local amplification of the barotropic tide relative to that in open water. The topographic Froude number, $Fr = U_0/Nh$, that compares a vertical length scale, U_0/N , of the stratified flow to the topographic height, h , is a parameter that is important not only in the case of oscillating flow but also for steady currents. In viscous flows, the Reynolds number is additionally important. The parameter, $Re_h = U_0 h/\nu$, is relevant for topography-scale features in the flow, while $Re_s = U_0 \sqrt{2\nu/\Omega}/\nu$ based on the Stokes boundary layer thickness is relevant to the oscillating boundary layer.

The excursion number, Ex , is generally small for large generation sites but can be large for smaller topographic features under energetic tides. An M2 tide (period of $T = 12.4$ h and $\Omega = 1.4 \times 10^{-4}$ s $^{-1}$) with an amplitude of 0.2 m s $^{-1}$ has an advection length scale $l = 1.4$ km. An ocean ridge with characteristic length scale of $l = 100$ km corresponds to a small $Ex = 0.014$, while a small topographic feature with $l = 1.4$ km corresponds to $Ex = 1$. If the barotropic cross-ridge velocity is even larger, e.g. 0.6 m s $^{-1}$ as can occur in shallower water, a characteristic length scale of $l = 4.2$ km corresponds to $Ex = 1$. The Froude number, $Fr = Ex(\Omega/N)/(h/l)$. For moderately steep topography with average slope angle comparable to the wave characteristic angle, it follows that $h/l = O(\Omega/N)$, leading to $Fr \simeq Ex$. We will investigate the dynamics of such topography over the range of low to $O(1)$ values of Ex and Fr .

Bell (1975a) developed a linear theory for topographic internal wave generation by oscillatory forcing, the so-called weak topography approximation (WTA), based on shallow slope, $\epsilon \ll 1$, and topography height much less than the vertical wavelength of the internal tide. The theory has been developed further by others (Balmforth, Ierley & Young 2002; Llewellyn Smith & Young 2002; St Laurent *et al.* 2003; Pétrélis, Llewellyn Smith & Young 2006; Echeverri & Peacock 2010) to progress beyond these simplifications in order to address more realistic cases with steeper slope and larger topographic height. Linear theory shows that the radiated wave flux (equal to the conversion from barotropic to internal wave energy in the linear inviscid approximation) is proportional to $(\pi/4)\rho_0 U_0^2 h^2 \sqrt{N^2 - \Omega^2}$, and leads to explicit values for the non-dimensional wave flux for different topographic shapes. Legg & Huijts (2006) employed two-dimensional simulations in the laminar flow regime ($Re_s \sim 10$) to investigate the problem for various tidal amplitude and topographic shapes, finding good agreement with several trends inferred from linear theory: scaling of radiated flux

with U_0^2 and h^2 , increased radiation in supercritical topography relative to subcritical, and appearance of high harmonics when the tidal excursion number is large.

Tall regions of $O(50\text{--}100)$ m with overturned isopycnals have been observed (Aucan *et al.* 2006; Levine & Boyd 2006; Klymak, Pinkel & Rainville 2008) at Kaena Ridge, a generation site in the Hawaiian Ridge system, and massive overturns up to 300 m tall have been reported by Alford *et al.* (2011) at Luzon Strait. Nonlinear effects and turbulence at wave generation sites, the primary subject of the present study, arise as a result of various factors. Consider topography with streamwise length scales large enough for low Ex , as is the case for large generation sites in the ocean. Nonlinear effects are possible at sloping regions that are locally critical, i.e. $\epsilon = 1$, where wave generation is a resonant process. At $\epsilon = 1$, the near-bottom velocity intensifies, giving rise to a laminar boundary layer (Gostiaux & Dauxois 2007; Zhang, King & Swinney 2008) at low Reynolds number or a thick turbulent boundary layer (Gayen & Sarkar 2010; Lim, Ivey & Jones 2010; Gayen & Sarkar 2011*b*) with cyclical overturns during flow reversal from down- to upslope flow when the Reynolds number exceeds a threshold, $Re_s \simeq 100$. The intensified boundary layer associated with an internal wave beam at topography can be a reason for the overturns observed by Aucan & Merrifield (2008) at deep locations on the ridge flank as suggested by the large eddy simulation of Gayen & Sarkar (2011*a*) and for the overturns observed on critical regions of the continental slope by Bluteau, Jones & Ivey (2011). Steep topography with supercritical slope can also lead to nonlinear features, particularly near the ridge crest. Legg & Klymak (2008) identify transient hydraulic jumps that occur at maximum offslope flow that, when the barotropic tide relaxes, move towards the slope and propagate upslope with overturned isopycnals, similar to the observations of Klymak *et al.* (2008) at Kaena Ridge. Supercriticality ($\epsilon > 3$) was identified by Legg & Klymak (2008) as a necessary condition for the overturns found in their numerical simulations. Flow at the obstacle is blocked below a location of depth $O(U_0/N)$ from the crest in the low- Fr regime. Winters & Armi (2013) introduced an inner length scale, l_{in} , to characterize the streamwise obstacle dimension at the blocking location and a corresponding inner excursion number, $Ex_{in} = U_0/\Omega l_{in}$. Supercritical topography with small outer excursion number, Ex , but $Ex_{in} = O(1)$, was found to have strong nonlinear and asymmetric flow response, hydraulic control near the crest and overturned eddies in the downstream supercritical ($Fr > 1$) flow. The two-dimensional form of the non-hydrostatic equations was used by both Legg & Klymak (2008) and Winters & Armi (2013). From observations and numerical simulations, it is clear that nonlinear wave processes and turbulent near-bottom layers are operative at near-critical and supercritical generation sites. This motivated the three-dimensional non-hydrostatic turbulence-resolving simulations by Rapaka, Gayen & Sarkar (2013), who examined oscillating flow over a model laboratory-scale triangular ridge in the low- Ex regime. The radiative flux in the simulations agreed well with linear predictions for subcritical topography but critical and supercritical cases with higher-amplitude forcing exhibited significant reduction in radiative flux, as much as 25%, with respect to linear estimates. Turbulence was found on both windward and leeward sides of the obstacle, exhibited a systematic dependence on tidal phase, and showed a substantial variation of spatial/temporal features as a function of its location on the ridge.

Energetic barotropic tides over small obstacles can lead to values of excursion number comparable to unity, a regime that was not considered by Rapaka *et al.* (2013). Lee waves, that form in the case of steady flow over topography, may occur as a transient feature. Flow separation and breaking lee waves (Baines 1995) lead to

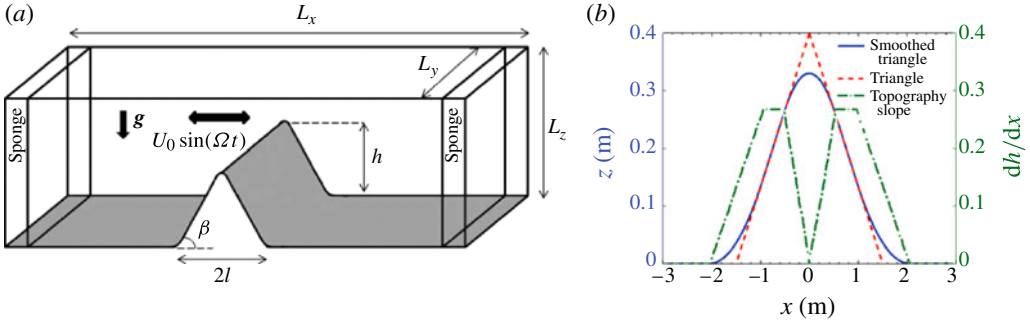


FIGURE 1. (Colour online) (a) Schematic of the problem (not to scale): stratified fluid oscillates over a two-dimensional obstacle. (b) Profiles of the smoothed triangular topography (solid line; blue online) used in the present work and the triangular topography (dashed line; red online) used by Pétrélis *et al.* (2006). The two truncated triangles (dashed line; green online) show the topography slope. Note that the constant slope region is critical with an angle of 15° and occupies 20% of the streamwise length.

turbulence in the steady case. These considerations motivate the present examination of values of Ex up to unity. We perform direct numerical simulations (DNS) of the full three-dimensional Navier–Stokes equations for a laboratory-scale model with a region having critical slope to examine the properties of internal waves with a focus on how these properties change with respect to the low- Ex regime.

2. Problem set-up

An oscillating tide over a two-dimensional obstacle, figure 1(a), is studied using fully nonlinear three-dimensional simulations. Background thermal stratification with a constant buoyancy frequency, N_∞ , is considered while the bottom surface is assumed to be adiabatic. The background barotropic current, $U(x) \sin(\phi)$, where ϕ is the tidal phase, is forced by an imposed horizontal pressure gradient that oscillates in time (t_d),

$$F_0(t_d) = \rho_0 U_0 \Omega \cos(\Omega t_d). \quad (2.1)$$

Quantities u , v and w denote velocity in the streamwise (x), spanwise (y) and vertical (z) directions, respectively. The obstacle shown in figure 1(b) is obtained by taking a triangular profile, equation (2.2) with $h_0 = 0.4$ and $l_0 = 1.5$, and then smoothing it. The height is 0.328 m and half-length, l_0 , is 1.9 m, similar to the profile used by Rapaka *et al.* (2013):

$$z(x) = \begin{cases} h_0 \left(1 - \frac{|x|}{l_0}\right) & \text{if } |x| \leq l_0, \\ 0 & \text{otherwise.} \end{cases} \quad (2.2)$$

2.1. Governing equations and numerical method

The following non-dimensional form of the Navier–Stokes equations with rotation neglected is numerically solved:

$$\nabla \cdot \mathbf{u} = 0, \quad (2.3a)$$

$$\frac{D\mathbf{u}}{Dt} = -\nabla p^* + \cos(t)\mathbf{i} + \frac{1}{Re}\nabla^2\mathbf{u} - B\rho^*\mathbf{k}, \quad (2.3b)$$

$$\frac{D\rho^*}{Dt} = \frac{1}{Re Pr}\nabla^2\rho^* + w. \quad (2.3c)$$

The fluid properties are molecular viscosity ν , thermal diffusivity κ and density ρ . Bold letters indicate vector variables and non-dimensional parameters are defined as

$$\left\{ \begin{array}{l} t = t_d\Omega, \quad \mathbf{x} = (x, y, z) = \frac{(x_d, y_d, z_d)}{U_0/\Omega}, \quad p^* = \frac{P_d^*}{\rho_0 U_0^2}, \\ \mathbf{u} = (u, v, w) = \frac{(u_d, v_d, w_d)}{U_0}, \quad \rho^* = \frac{\rho_d^*}{\frac{U_0}{\Omega} \left. \frac{d\rho_d}{dz_d} \right|_{\infty}}. \end{array} \right. \quad (2.4)$$

Here, p^* denotes deviation from the background hydrostatic pressure and ρ^* denotes the deviation from the linear background state, $\rho_b(z)$. There are three non-dimensional parameters in the governing equations: Reynolds number Re , buoyancy parameter B , and Prandtl number Pr defined as

$$Re \equiv \frac{l_{ex}U_0}{\nu} = \frac{U_0^2}{\Omega\nu}, \quad B \equiv -g \left. \frac{d\rho_d^b}{dz_d} \right|_{\infty} \frac{1}{\rho_0\Omega^2} = \frac{N_{\infty}^2}{\Omega^2}, \quad Pr \equiv \frac{\nu}{\kappa}, \quad (2.5a-c)$$

where $l_{ex} = U_0/\Omega$ is the tidal excursion length and N_{∞} is the background value of buoyancy frequency, assumed to be constant. It is common to use the Reynolds number based on the Stokes boundary layer thickness, $\delta_s = \sqrt{2\nu/\Omega}$,

$$Re_s = \frac{U\delta_s}{\nu} = \sqrt{2Re}, \quad (2.6)$$

as an alternative to Re . Using all the geometry-dependent parameters, there are three other independent non-dimensional parameters in addition to those listed in (2.5): the excursion number $Ex = U_0/(l\Omega)$, the slope angle β and the slope criticality parameter $\epsilon = \tan(\beta)/\tan(\theta)$, where θ is the angle of internal wave phase lines with the horizontal given in a non-rotating environment by $\theta = \tan^{-1} \sqrt{\Omega^2/(N_{\infty}^2 - \Omega^2)}$. The topographic Froude number, $Fr = U_0/(N_{\infty}h)$, is also of interest. Since $Fr = Ex(\Omega/N_{\infty})(l/h)$, it is not independent of the previously listed non-dimensional parameters.

The governing equations (2.3) are written in generalized curvilinear coordinates as described by Gayen & Sarkar (2011b) and solved on a body conforming grid. A mixed finite-difference/spectral discretization, a third-order Runge–Kutta–Wray time advance, a fractional step method for the Navier–Stokes equations, and a multigrid Poisson solver for the pressure are employed. The numerical algorithm is described by Gayen & Sarkar (2011b) and specifics regarding the flow past an obstacle are given by Rapaka *et al.* (2013).

2.2. Baroclinic energy budget

The baroclinic energy equation is employed as the framework for investigating the energetics of the internal waves. In the case of linear inviscid theory, all the energy converted from the barotropic (Bt) to the baroclinic (Bc) wavefield is assumed to reside in the internal wavefield, i.e. Bt–Bc conversion and radiation terms are assumed

equal. However, the present fully nonlinear DNS enables relaxation of this simplifying assumption and separate quantification of the other key terms in the balance including the local dissipation and the flux that is advected rather than being radiated as the pressure work. Rapaka *et al.* (2013) revised the baroclinic energy equation of Carter *et al.* (2008) and Kang & Fringer (2012), splitting the velocity into a mean field, including barotropic and baroclinic components, and a three-dimensional fluctuation field:

$$u(x, y, z, t) = \langle u \rangle(x, z, t) + u'(x, y, z, t) = U + u_{bc} + u', \quad (2.7)$$

$$w(x, y, z, t) = \langle w \rangle(x, z, t) + w'(x, y, z, t) = W + w_{bc} + w'. \quad (2.8)$$

Similarly, pressure was decomposed as $\langle p^* \rangle = P^* + p_{bc} + p'$, where p^* stands for the deviation from hydrostatic pressure. Here, symbol $\langle \rangle$ indicates spanwise averaging; and U, P^*, W are the barotropic components, the first two being the depth averages of $\langle u \rangle$ and $\langle p^* \rangle$, respectively, and $W(z) = -(\partial/\partial x)[z - h(x)]U$. The terms u_{bc}, w_{bc} and p_{bc} are baroclinic components.

For $Re_s \gg 1$, the diffusive fluxes of wave energy can be neglected and the equation for the baroclinic energy without diffusive fluxes is simplified to

$$\frac{\partial}{\partial t}(\overline{E_k} + \overline{E_p}) + \nabla \cdot \overline{\mathbf{F}} = \overline{C} - \overline{\varepsilon_{bc}} - \overline{P}. \quad (2.9)$$

The terms can be written in more detail as:

$$\begin{aligned} \text{unsteadiness} & \quad \frac{\partial}{\partial t}(\overline{E_k} + \overline{E_p}), \\ \text{pressure flux } (M) & \quad \nabla_H \cdot (\overline{\mathbf{u}_{bcH} p^*}), \\ \text{advection flux } (M_{adv}) & \quad \nabla_H \cdot (\overline{\mathbf{u}_H(E_p + E_k)} + \overline{\mathbf{u}_{bcH} E_{hk}}), \\ \text{dissipation } (\varepsilon_{bc}) & \quad \rho_0 \nu \frac{\partial (\overline{\mathbf{u}_{bc}})_i}{\partial x_j} \frac{\partial (\overline{\mathbf{u}_{bc}})_i}{\partial x_j}, \\ \text{turbulence production } (P) & \quad -\overline{\langle u'_i u'_j \rangle_y \langle S_{ij} \rangle_y}, \\ \text{conversion } (C) & \quad -\frac{\partial \overline{p^*}}{\partial z} W, \\ \text{nonlinear conversion } (C_{nl}) & \quad \rho_0 H (\overline{U \nabla_H \cdot (\mathbf{u}_{bcH} \mathbf{u}_{bc})} + \overline{V \nabla_H \cdot (\mathbf{u}_{bcH} \mathbf{v}_{bc})}), \end{aligned}$$

where overbars represent depth integration, subscript H denotes horizontal, and

$$E_k = \frac{1}{2} \rho_0 (u_{bc}^2 + v_{bc}^2 + w_{bc}^2), \quad E_p = \frac{1}{2} N_\infty^{-2} b^2, \quad E_{hk} = \rho_0 (U u_{bc} + V v_{bc}). \quad (2.10a-c)$$

The buoyancy term, b , is defined as $b \equiv -g\rho^*/\rho_0$ and the rate-of-strain tensor, S_{ij} , is defined as $S_{ij} \equiv \frac{1}{2}(\partial U_i/\partial x_j + \partial U_j/\partial x_i)$. The energy flux, $\nabla \cdot \overline{\mathbf{F}}$, in (2.9) is expressed as the sum of the wave flux, M , and the advective flux, M_{adv} , in order to keep our notation consistent with the literature. Boundary conditions corresponding to a two-dimensional topography are used to simplify the equation. Symbol C represents conversion from the barotropic to the baroclinic wavefield, ε_{bc} represents viscous dissipation of the baroclinic energy. The nonlinear part of conversion, C_{nl} , and the advection flux, M_{adv} , were not considered by Rapaka *et al.* (2013), but are required in this study because of high Ex . The term, $-P$, is also considered as described in

Case	Re_s	Ex	Fr	N_x	N_y	N_z
CEX1	177	0.066	0.098	897	128	321
CEX2	177	0.200	0.300	897	128	321
CEX3	177	0.400	0.600	897	128	321
CEX4	177	0.700	1.026	897	128	321
CEX5	177	1.000	1.500	897	128	321

TABLE 1. Parameters of the simulated cases. In cases CEX1–CEX5, Ex number changes while Re_s is kept constant. For all cases: $L_x = 40$ m, $L_y = 0.5$ m, $L_z = H = 3.28$ m, $l = 1.9$ m, $h = 0.328$ m, $\beta = 15^\circ$, $\theta = 15^\circ$, $\Omega = 1$ s⁻¹, $\epsilon = 1$, $N_\infty^2 = 14.93$ s⁻² and $Pr = 1$.

Rapaka *et al.* (2013) to account for turbulence production, which represents local conversion from the internal tide to turbulence. Equation (2.9) can be reorganized to

$$C + C_{nl} = \frac{\partial}{\partial t}(E_p + E_k) + M + M_{adv} + \varepsilon_{bc} + P, \quad (2.11)$$

to give the following physical interpretation. Consider the integral of (2.11) over a domain enclosing the generation site and over a few tidal cycles. The net energy conversion ($C + C_{nl}$) from the barotropic tide is: (a) dissipated by viscosity (ε_{bc}) or converted to turbulence (P), (b) leaves the generation site as an internal wave flux (M) plus an advective flux (M_{adv}), and (c) leads to a temporal change in baroclinic energy content whose cyclic integral is close to zero if the state is close to being statistically steady.

2.3. Selection of simulations

Table 1 shows the principal parameters of the simulations. Five cases are studied in a series where Ex is changed, keeping other non-dimensional parameters constant. The value of Ex is changed from 0.066 to unity, a relatively high Ex . The large value of $Ex = 1$ is appropriate for energetic tides over small-scale obstacles in the ocean. For example, an M2 tide (period of $T = 12.4$ h and $\Omega = 1.4 \times 10^{-4}$ s⁻¹) with an amplitude of 0.2 m s⁻¹ flowing over an obstacle with half-length of 1.42 km would lead to Ex of unity. The obstacle chosen here has a smoothed triangular shape that is moderately steep with 20% slope length that is critical and blends smoothly into a subcritical region. The value of $Re_s = 177$ is larger than has been investigated in the laboratory experiments, is much smaller than oceanic values, but has the advantage of allowing DNS while being sufficiently large for turbulence. The wave angle of 15° with respect to the horizontal is smaller than in most laboratory experiments but still approximately 2–3 times larger than typical values in the ocean.

The turbulent fluctuations are inferred via departures of instantaneous velocity, pressure and density from the spanwise average. Statistics of turbulent quantities are a function of x and z , and are computed by spanwise averaging. The computational domain lengths in the horizontal directions, L_x and L_y , and the vertical domain length, L_z , are specified in table 1. The spanwise domain length, L_y , is chosen so as to accommodate the largest spanwise vortical structures that appear during convective instability. A grid with approximately 36 million grid points is used and designed to have adequate resolution of boundary layer turbulence and good resolution of turbulence arising from convective overturns and wave breaking. Case CEX1 has the first grid point from the wall at $z_1^+ = 2$ (distance normalized by the viscous wall unit ν/u_τ). Minimum grid resolution in the streamwise direction (Δx_{\min}^+) is 21 and the

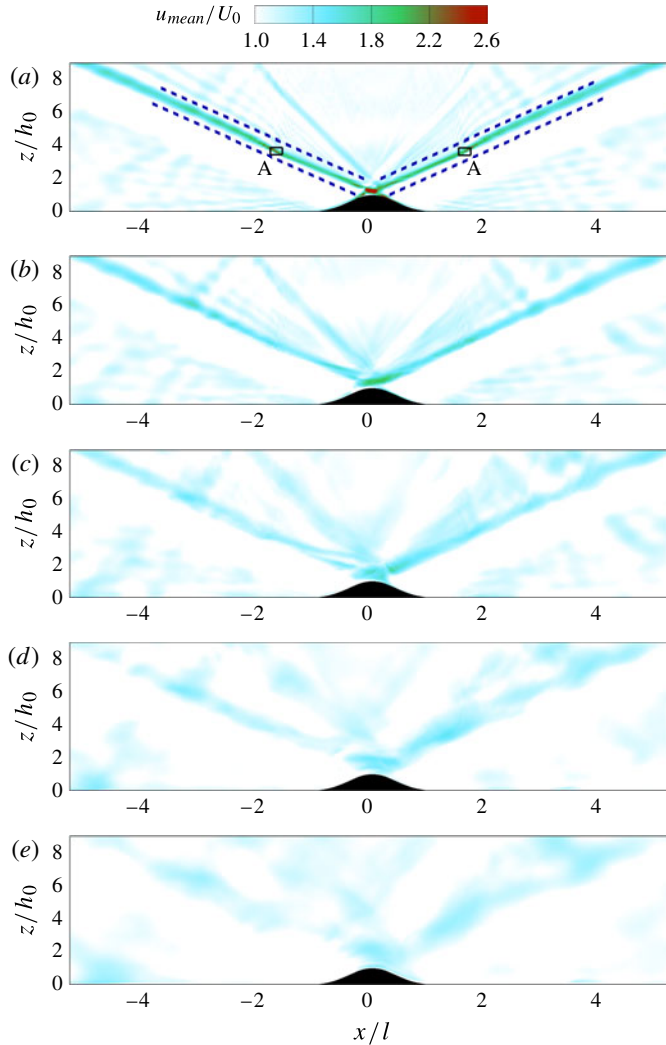


FIGURE 2. (Colour online) Instantaneous streamwise velocity at $t/T = 6.25$ and phase, $\phi = \pi/2$, corresponding to positive peak in barotropic velocity: (a) $Ex = 0.066$, (b) $Ex = 0.2$, (c) $Ex = 0.4$, (d) $Ex = 0.7$ and (e) $Ex = 1.0$. Topography is shown in black, and beam regions are shown between dashed line at each side in (a).

spanwise direction has a uniform grid spacing of $\Delta y^+ = 16$ with spatial derivatives computed with spectral accuracy. The long integration time (approximately 10 cycles) is computationally expensive, e.g. approximately 9000 time steps are used per cycle for the $Ex = 1$ case.

3. Characteristics of the internal wavefield

The spatial structure of the internal wavefield changes with Ex . At $Ex = 0.066$ (figure 2a), the internal wave response exhibits a coherent internal wave beam with fluid velocity that is substantially larger than the barotropic background velocity and an angle corresponding to the barotropic forcing, Ω . Rays with angles corresponding

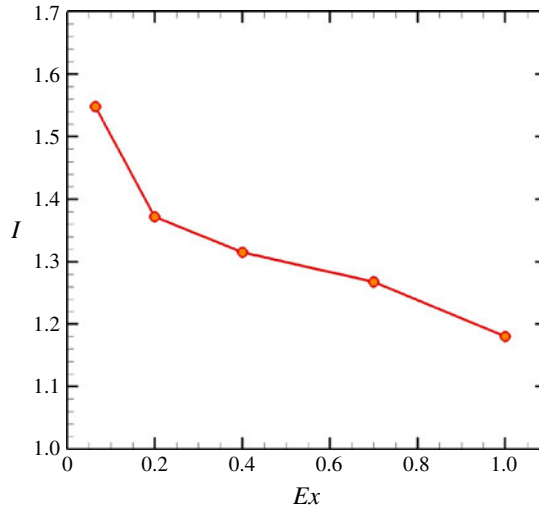


FIGURE 3. (Colour online) The dependence of velocity intensification, I , in the internal wave beam on excursion number. Here, $I = (1/A) \int u_b/U_0 dA$, where u_b is the velocity amplitude in the beam region at $x/l \sim 2$ (shown in figure 2*a* with symbol A) and A is the area of the beam region.

to harmonics and interharmonics can also be seen. However, with increasing Ex , the internal wave beam becomes less coherent and exhibits smaller velocity intensification. The wave response also becomes progressively more asymmetric, with the beam pattern shifting towards the lee of the obstacle. When the slope angle is critical and equal to the characteristic angle of wave propagation in the stratified background, the local baroclinic response is resonant, leading to intensification of near-bottom velocity. The model topography chosen here has a slope length $l_c/l = 0.2$ at each flank. At low Ex , a fluid particle on the critical slope is exposed to a slope angle that is critical throughout its oscillation, leading to the strong velocity intensification seen in figure 2(*a*). At larger Ex , the fluid particles that are nominally on the critical slope are advected on to regions with subcritical slope angle, thus weakening the resonant response. The attenuation of normalized fluid velocity in the beam with increasing Ex is quantified in figure 3. We expect qualitative similarities between the behaviour of the intensification and the normalized wave flux, M , because the latter depends on the amplitude of the oscillating fluid velocity.

Steady flow over an obstacle, in the appropriate Froude-number regime, can lead to lee waves that are standing wave patterns in the lee of the obstacle. When the oscillatory tide has $Ex = O(1)$, analogous wave patterns are formed in the lee of the obstacle with phase lines that are different from the beams present at low Ex . The case with $Ex = 1$ simulated here shows isopycnals with large displacements that extend to significant vertical and horizontal distances from the obstacle. The lee waves generated near the topography in each half-cycle are responsible for these displacements. To obtain a clear picture of the life cycle of lee waves generated by oscillatory flow, it is beneficial to follow a wave phase line. The waves are released every half-cycle at the lee side of the obstacle when the leeward flow reverses and the velocity passes through zero. Consider line A (figure 4*a* on the right flank) that forms at phase 180° , the end of the half-cycle with positive velocity, during which the right flank is in the

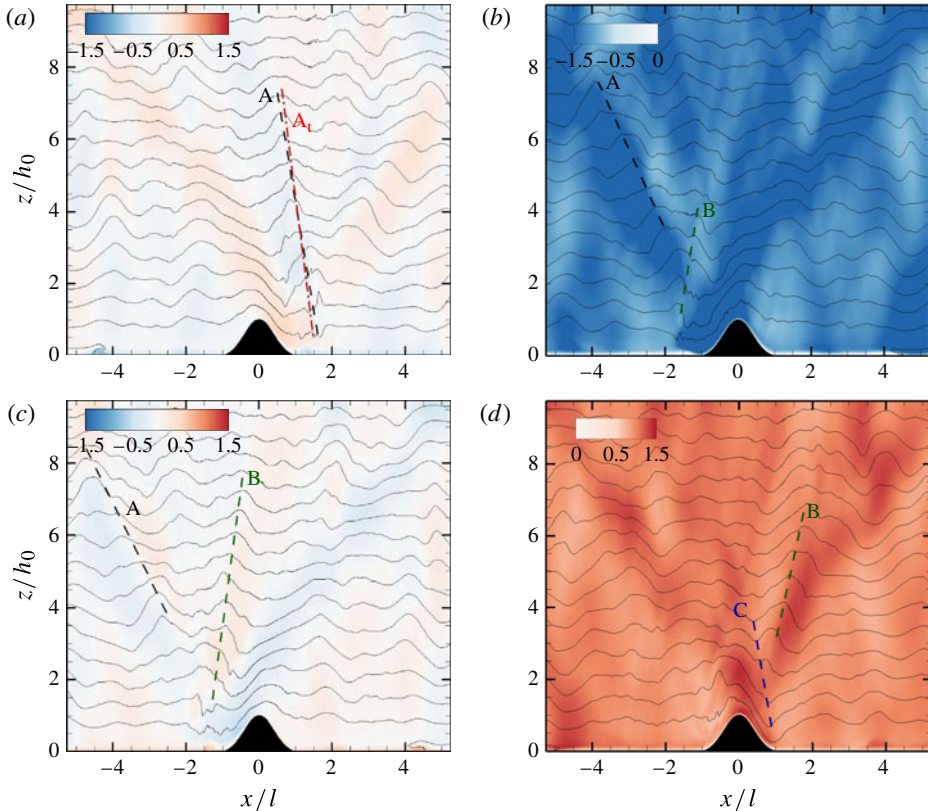


FIGURE 4. (Colour online) Normalized streamwise velocity and isopycnals in case CEX5 ($Ex = 1.0$) for: (a) $t/T = 5.5$, phase 180° when $U_0 = 0$; (b) $t/T = 5.75$, phase 270° at peak U_0 ; (c) $t/T = 6$, phase 0° ; and (d) $t/T = 6.25$, phase 90° . The life cycle of a lee wave is illustrated through phase lines A, B and C. The line A_t shows a phase line obtained from linear theory using the barotropic velocity amplitude and obstacle length.

lee of the oscillating tide. The inclination, θ_A , of phase line A with the horizontal can be estimated from linear theory as follows. A current of velocity U_0 flowing over a periodic bump of wavelength $\lambda = 2l$ gives rise to a wave with frequency $\omega = U_0\pi/l$ so that

$$\sin(\theta_A) = \omega/N = U_0\pi/lN = \pi Ex \sin \theta, \quad (3.1)$$

where θ is the angle of the internal wave beam with the horizontal. Equation (3.1) with the parameters of case CEX5 leads to $\theta_A = 54.4^\circ$, which, as shown in figure 4, agrees well with the inclination of the lee wave phase line in the simulation. It is interesting to note that, at $Ex = 1/\pi$, the inclination of the lee wave phase line is equal to that of a freely propagating internal wave ray and therefore conducive to an intensified wave response.

Line A is born and can be taken to be an initial phase line for the subsequent flow during the very next half-cycle when the right flank becomes windward. Line A is advected from the windward side to the leeward side while another lee wave phase line is being generated, e.g. line B in figure 4(b). As shown in figure 4(b), the displacement that was initially present in the lower part of line A fades; this is because the lee wave breaks at the topography, leading to turbulence, as will be

discussed in the following section. Figure 4(c) corresponds to phase 0° at which time the angle of line A changes because it advects into the region corresponding to a wave beam. The 0° phase corresponds to the end of leeward flow on the left flank and, accordingly, the lee wave on the left flank is fully formed as shown by phase line B. Figure 4(d) shows a phase of 90° . Line B has advected across and beyond the obstacle, and a new wave is being formed on the right side of the topography as shown by phase line C. However, line A at phase 180° with which we initiated the discussion is no longer identifiable. Thus, a lee wave phase line is very clear during half a cycle, from flow reversal at one flank to flow reversal at the other flank.

4. Energetics of the baroclinic response

The baroclinic energy budget is quantified to assess the change in wave energetics among cases CEX1 to CEX5. The contribution of each term in (2.11) is shown in table 2. The terms of the normalized budget shown in table 2 are also plotted in figure 5(a) as a function of Ex . The primary inference to be drawn from this figure is the considerable drop in radiated wave flux, M . The increase in the advection term, M_{adv} , and the increase in baroclinic dissipation term, ε_{bc} , lead to both terms drawing more energy from the conversion C , leaving less available for radiation. Furthermore, C also decreases somewhat with increasing Ex . The larger barotropic forcing velocity U_0 leads to an increase in the advection term, M_{adv} , which is not surprising since M_{adv} is proportional to the velocity cubed while the normalization factor is proportional to the velocity squared. The increasing importance of M_{adv} can also be explained as follows. In the linear case, there is a strong correlation between pressure and velocity. It can be recognized in the governing equation (2.3) because, in the absence of nonlinear terms and molecular dissipation, the imposed pressure gradient term, ∇p^* , is fully used to accelerate a fluid particle, du/dt . Increasing the horizontal excursion of the barotropic background flow implies that a part of the pressure gradient term can no longer be used to locally accelerate the fluid particle but instead accounts for fluid inertia, $\mathbf{u}_0 \cdot \nabla \mathbf{u}$.

Assuming that the length scale of the velocity gradient remains constant among cases leads to the normalized baroclinic dissipation being proportional to $1/Re_s$. In the present simulations, Re_s is held constant but the normalized dissipation increases with increasing Ex . The reason is the enhancement in small scales associated with nonlinear wave steepening and wave breaking, as well as a larger horizontal extent of the dissipative region when the excursion number increases.

The conversion, C , from barotropic to baroclinic energy decreases somewhat (almost 8% at $Ex = 1$), although not as much as the decrease in M (almost 25% at $Ex = 1$), with increasing excursion number. It is also worth examining the widely used linear estimate of Bt–Bc energy conversion, which simplifies the conversion term to the time average of the following equation using the pressure and velocity from numerical simulation:

$$C^* = \int_x p^*(x, 0, t) U(x, 0, t) \frac{dh}{dx} dx. \quad (4.1)$$

Figure 5(b) shows the estimate of simplified conversion as well as the contributions from hydrostatic and non-hydrostatic pressure to this estimate. The simplified conversion shows little change with increasing Ex , while the hydrostatic component increases with Ex . Reduction in the non-hydrostatic part compensates for the increase in the hydrostatic component and makes C^* approximately invariant to Ex . The hydrostatic pressure is computed using the density fluctuation from the background

Case	Ex	Tendency	Conversion to waves (C)	Wave flux (M)	Baroclinic dissipation (ε_{bc})	Turbulent production (P)	Advection flux (M_{ad})	Nonlinear conversion (C_{nl})	Residual
CEX1	0.066	0.00291	0.622	0.555	0.0141	0.0350	0.00221	0.00102	0.0187
CEX2	0.2	0.00838	0.598	0.511	0.0350	0.0276	0.01493	0.00374	0.0050
CEX3	0.4	0.00109	0.574	0.463	0.0540	0.0215	0.04961	0.01540	-0.0009
CEX4	0.7	-0.00285	0.604	0.474	0.0861	0.0184	0.07339	0.02249	-0.0228
CEX5	1.0	0.00259	0.574	0.416	0.1185	0.0141	0.11418	0.03337	-0.0585

TABLE 2. Baroclinic energy budget. Each term in (2.11) is integrated over a box spanning $-1.57 < x/l < 1.57$ in the horizontal direction, averaged over the forcing time period at statistical steady state, and normalized by the factor $(\pi/4)\rho_0 U_0^2 l_0^2 \sqrt{N^2 - \omega_0^2}$ that appears in simplified analysis.

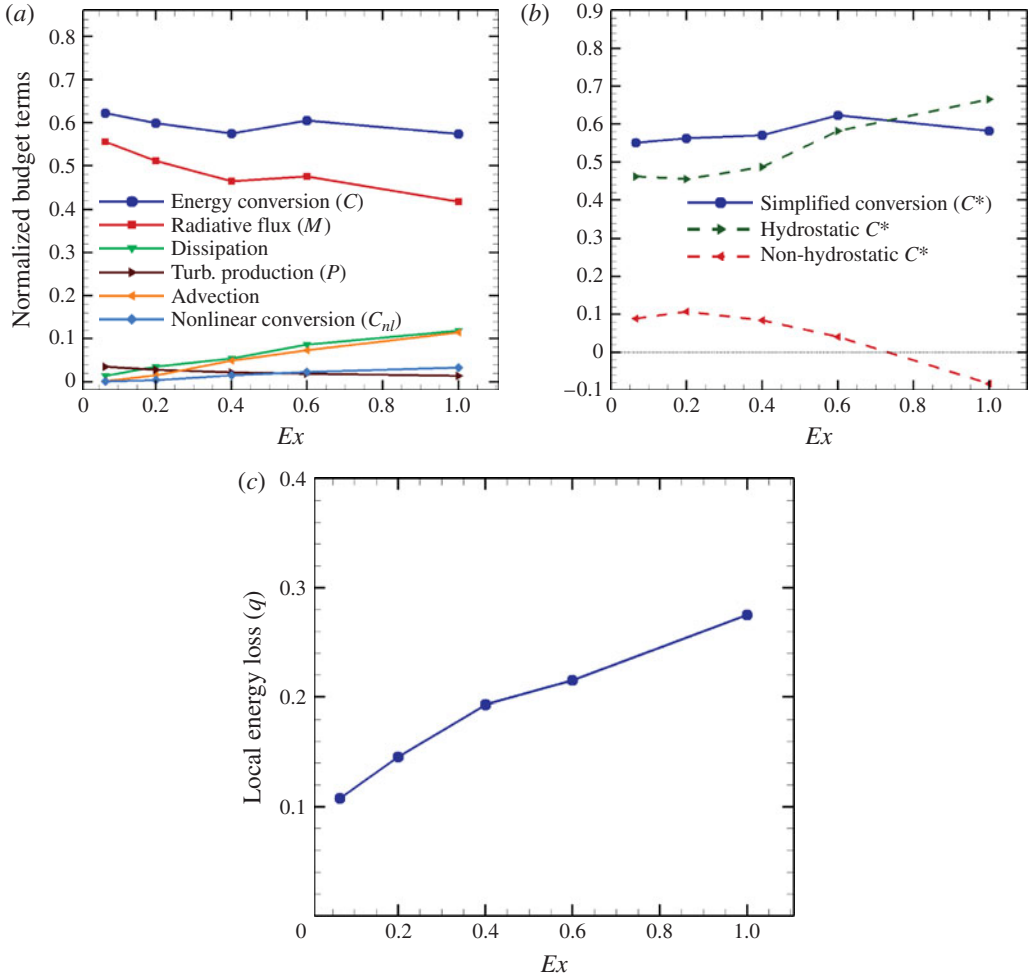


FIGURE 5. (Colour online) Effect of Ex on (a) baroclinic energy budget terms, and (b) simplified conversion term along with its hydrostatic and non-hydrostatic components. All terms are integrated between $x/l = \pm 1.57$ and normalized by $(\pi/4)\rho_0 U^2 h^2 \sqrt{(N^2 - \Omega^2)}$. (c) Local loss of internal wave energy, $q = 1 - M/C$.

and subsequently the hydrostatic component is calculated as the time average of $\int_x (\int_z \rho^*(x, z, t) g dz) U_0 (dh/dx) dx$.

Internal tides are thought to be an important contributor to mixing in the ocean interior. Therefore, the fractional amount of barotropic energy converted to baroclinic energy at topography that escapes as radiated internal waves is of interest. The quantity, $q = 1 - M/C$, is plotted in figure 5(c). The local loss, q , increases to almost 0.3 at $Ex = 1$, a value that is three times the value at low Ex .

We now discuss the spatial organization of the cycle-averaged terms involved in the baroclinic energy balance plotted in figure 6(a–l). Each term in figure 6 shows a substantial decrease in the coherence of the beam pattern when Ex increases so that, in the cycle-averaged view, the beam is virtually absent at $Ex = 1$. The spatial organization of conversion is significantly affected by the excursion number. When

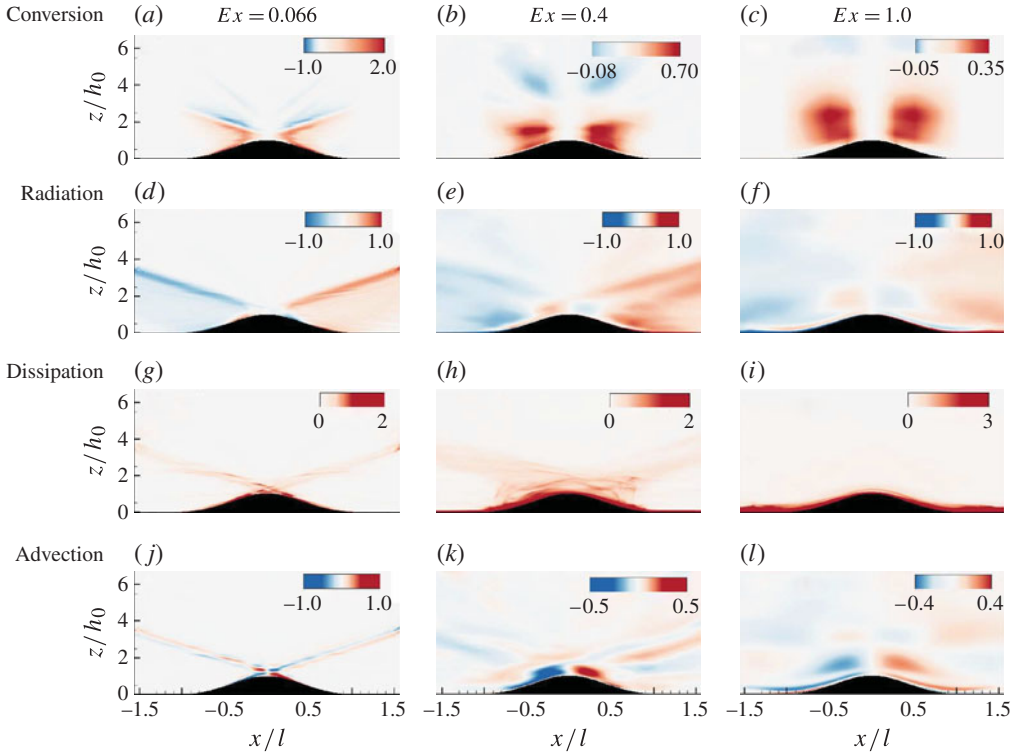


FIGURE 6. The spatial organization of cycle-averaged terms in the baroclinic energy balance normalized by $(\pi/4)\rho_0 U_0^2 h_0^2 \sqrt{N^2 - \omega_0^2}$.

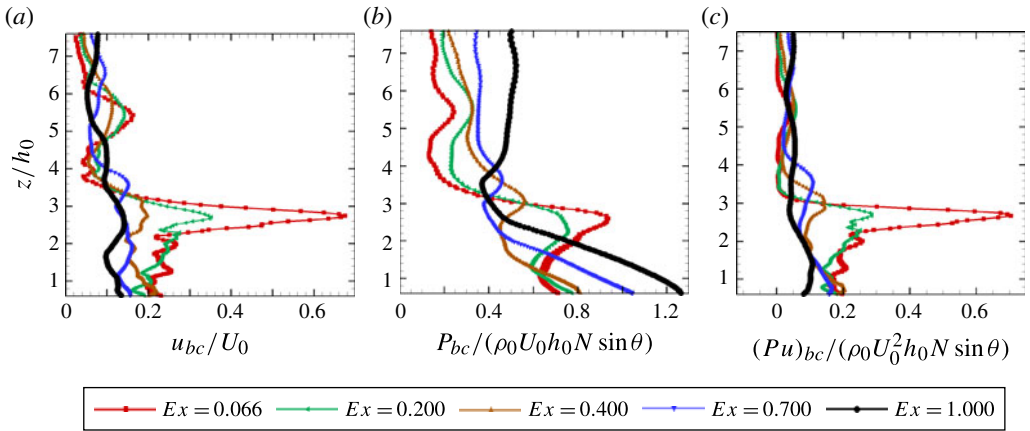


FIGURE 7. Vertical profiles of the normalized values of (a) the baroclinic velocity amplitude, (b) the baroclinic pressure amplitude, and (c) the amplitude of the pressure-velocity correlation. Profiles are shown at $x/l = -1$ for different Ex .

Ex increases, a larger area is involved in the Bt–Bc conversion, whereas, at low Ex , the conversion is dominant at the beams. It is remarkable that, although the spatial organization of the conversion term (figure 6*a–c*) changes dramatically with increasing Ex , the change in its spatially integrated value in figure 5(*a*) is small and consistent with the trend in the linear estimate obtained from the boundary forcing. The dissipation plots are also noteworthy. As shown in figure 6(*g*), baroclinic dissipation at low Ex occurs mainly in the boundary layer at critical slope and in the beams, both near the obstacle top and in the radiated tails. On the other hand, in the larger $Ex = 1$ case, baroclinic dissipation dwindles in the beam area and strengthens near the bottom, both at the sloping topography and the neighbouring flat bottom region owing to breaking lee waves, as will be discussed later. For better understanding of the decrease in M and C , the vertical profile of the amplitude of u_{bc} and P^* , and the amplitude of the correlation, $(P^*u)_{bc}$, computed at $x/l = -1$ are plotted. Figure 7(*a*) confirms the previous discussion about diminished beam structure in the baroclinic velocity. Although the baroclinic pressure decreases in the beam region with increasing Ex , the magnitude at the boundary increases.

5. Turbulence

Figure 8(*a–f*) shows snapshots of the near-field flow, each showing turbulent kinetic energy (TKE), isopycnals and velocity profiles. Note that $TKE = 0.5(u_{rms}^2 + v_{rms}^2 + w_{rms}^2)$ with subscript *rms* denoting root mean square. Three cases with $Ex = 0.066$, $Ex = 0.4$ and $Ex = 1.0$, respectively, are arranged as three rows, with each row showing two phases of the flow. The left column corresponds to a phase when the flow turns from leftward to rightward or slightly past that point, and the right column corresponds to peak rightward velocity (phase 90°) with the expectation of quasi-symmetric behaviour at phase 180° and phase 270° . At low Ex (figure 8*a–b*), TKE is present on the slopes, above the top of the obstacle as well as in the internal wave beam radiated away. At $\phi = 0^\circ$, there is a turbulence layer over and parallel to the left slope with a characteristic thickness equal to that of the overturned isopycnals in that region.

Intensification of the boundary flow at the critical slope (Gayen & Sarkar 2011*b*) that leads to convective instability during flow reversal from down- to upslope (Gayen & Sarkar 2011*a*) is the underlying mechanism for transition to turbulence. These fluctuations then interact with the shear of the accelerating upslope flow to drive TKE. A quarter cycle later when the barotropic velocity peaks at $\phi = 90^\circ$ (figure 8*b*), the turbulence patch is near the crest and again has a thickness equal to that of the overturned isopycnal. The TKE above the topography is bounded by the two internal wave beams that radiate upwards from the flanks.

In moving from $Ex = 0.066$ to larger Ex numbers, there is a qualitative change in the turbulence. At $Ex = 0.4$, the patch of intense TKE (figure 8*c*) becomes much taller, extending from the bottom to approximately twice the topographic height and, instead of being oriented parallel to the slope, is almost vertical. The isopycnals are indicative of a tall convective overturn of height approximately $2h_0$. The wave response (figure 2) was shown to be increasingly asymmetric with respect to the centre with increasing Ex and so is the TKE pattern; owing to the leftward flow preceding $\phi = 0^\circ$, turbulence is displaced increasingly to the left (leeward) side. A rightward moving wave is released when the leeward flow slows down, isopycnals exhibit large-amplitude deformation, and the generated lee waves break, leading to turbulence, e.g. the tall and intense TKE patch at $x/l \sim -0.8$ in figure 8(*c*). Note that the phase of 20° that is shown in figure 8(*c*) allows sufficient time for TKE to develop from the convective instability that occurs slightly earlier at a phase of 0° . Turbulence present at $\phi = 20^\circ$ advects

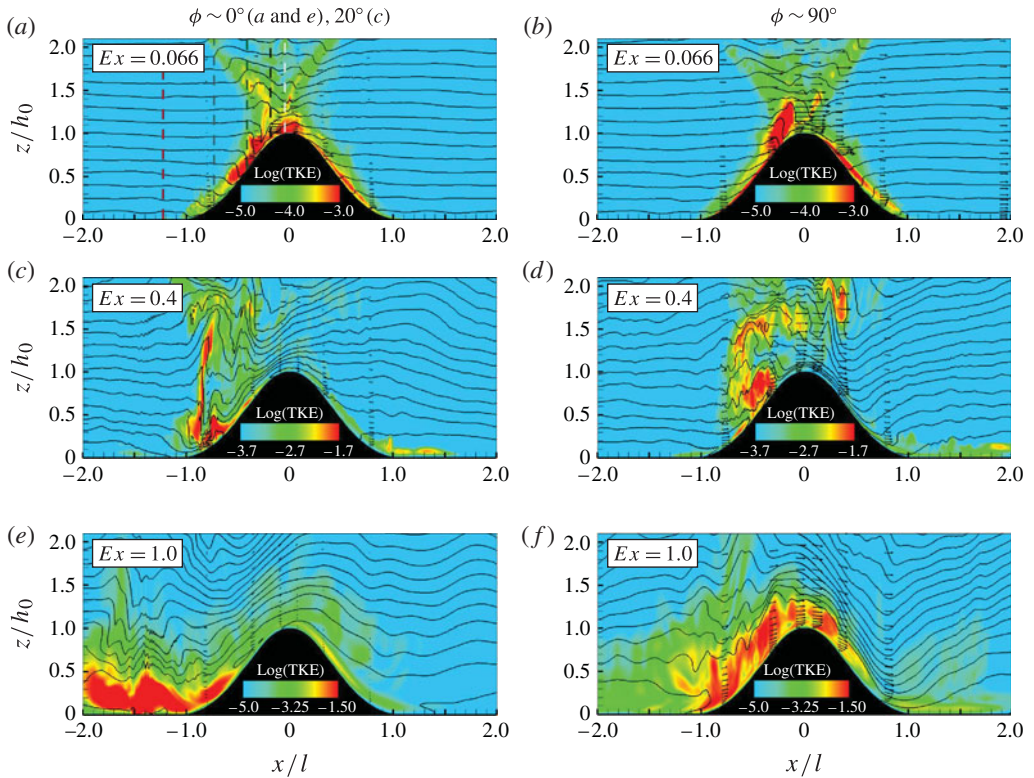


FIGURE 8. Snapshots of TKE (not normalized) and isopycnals. Panels (a,c,e) correspond to a phase of zero or small positive value of barotropic velocity, while panels (b,d,f) correspond to a positive peak of barotropic velocity: (a) $Ex = 0.066$ at $t/T = 6$; (b) $Ex = 0.066$ at $t/T = 6.25$; (c) $Ex = 0.4$ at $t/T = 6.05$; (d) $Ex = 0.4$ at $t/T = 6.25$; (e) $Ex = 1.0$ at $t/T = 6$; and (f) $Ex = 1.0$ at $t/T = 6.25$. Velocity vectors are also shown at selected cross-sections.

upslope and there are additional smaller patches of TKE above the obstacle at the later time shown in figure 8(d). Since the beams are no longer thin and strong, the smaller patches of turbulence are not clearly clustered along characteristic ray paths.

There is a further change in the spatial pattern of turbulence at $Ex = 1$. Although the vertical displacement of isopycnals is as large as at $Ex = 0.4$, the height of the TKE patches in figure 8(e-f) is not as large. Since a fluid particle sweeps back and forth across the entire topographic feature when Ex is unity, the critical angle present at only 20% of the length is unable to significantly intensify the baroclinic velocity unlike at low Ex . Therefore, in spite of the large fluid velocity, the internal wave shear is not large away from the boundary. Turbulence is dominant in a bottom boundary layer (figure 8e) with weakly stratified fluid and large shear in the lee wave response. Later in time, the weakly stratified layer of turbulence advects upslope. When the barotropic velocity is positive and at maximum (figure 8f), TKE is present over the entire windward slope.

Overtaken lee waves and turbulence high above an obstacle can occur in the case of steady currents as discussed by Baines (1995) and by the numerical investigations of Afanasyev & Peltier (1998) and Yakovenko, Thomas & Castro (2011). Here, the lee wave displacements in the $Ex = O(1)$ cases extend high above the obstacle but do

not overturn. A likely reason is that the duration, $T/2$, of unidirectional flow is not sufficiently long. The non-dimensional time corresponding to a half-period is

$$\frac{U_0 T}{2h} = \frac{U_0 \pi}{\Omega h} = \frac{\pi Ex}{A}, \quad (5.1)$$

where $A = h/l$ is the aspect ratio of the obstacle. The simulations of Yakovenko *et al.* (2011) conducted at $Fr = 0.6$ required $U_0 t/h \sim 22.5$ for overturning and $U_0 t/h \sim 40$ for a fully developed patch of turbulence. Since $A \simeq 0.2$ and $Ex \leq 1$ in the present simulations, the lee waves do not have sufficient time to overturn and break down into turbulence. Nevertheless, overturning aloft the obstacle may be possible at smaller values of A and also when Fr is smaller, leading to stronger nonlinearity associated with the bottom boundary.

The gradient Richardson number, $Ri_g(x, z) = N^2(x, z)/S^2(x, z)$, where S is the mean (span-averaged) shear and N is mean (span-averaged) buoyancy frequency, is an indicator of possible instability. Convective instability ($Ri_g(x, z) < 0$) and shear instability ($0 < Ri_g(x, z) < 0.25$) at the phases corresponding to the snapshots shown in figure 8 are shown in figure 9. When $Ex = 0.066$, the convective instability associated with flow reversal ($\phi = 0^\circ$) is clearly present at $x/l \sim -0.5$, the region where the slope is critical, and advects to a somewhat higher location at $\phi = 90^\circ$. There are also convective and shear unstable regions in the narrow region adjacent to the sides of the topography, particularly in the downward beam at the leeward side, associated with shear in the high-mode baroclinic response.

In addition, the crossing of the two beams radiated from the opposite sides leads to unstable regions at the crest. Small regions of shear instability in the upward beams are also noticeable, even as high as $z/h \sim 1.4$, in figure 9(b), and they lead to turbulence in the beams, as discussed later.

At a larger value of $Ex = 0.4$ (figure 9c), there is a tall convectively unstable region with $Ri_g < 0$ located at $x/l \sim -0.9$, bounded from below by the bottom, and from above by the beam launched from the opposite flank of the topography. This convective instability at $\phi = 0^\circ$ is responsible for transition to turbulence that evolves into the tall patch of TKE at $\phi = 20^\circ$ that was seen at $x/l \sim -0.8$ in figure 8(c). Because of the subsequent rightward propagation of the wavefield, patches of convective and shear instability can be seen to span a large area between the topography and the beams in figure 9(d). In addition, convective and shear instabilities occur in the boundary layer at both phases shown for $Ex = 0.4$. When the tidal forcing is further increased so that $Ex = 1.0$, shear instability in the boundary layer dominates as shown in figure 9(e–f), although there are interspersed convectively unstable spots indicative of overturns. The regions with $0.25 < Ri_g < 5.0$ above the near-bottom turbulent layer have weaker TKE with patterns that are similar between $Ex = 0.4$ and $Ex = 1.0$, as can be seen by comparing panels (e) and (f) of figure 9 with panels (c) and (d), respectively.

The spatial organization of cycle-averaged TKE in figure 10 changes dramatically with increasing Ex . Turbulence is concentrated on the upper slope (the critical region and above it) and along the internal wave beams at lower $Ex = 0.066$, is concentrated at and above the lower slope in the $Ex = 0.4$ case, and is concentrated at the flat bottom adjacent to the obstacle and in an envelope around the obstacle at $Ex = 1.0$. When normalized by the kinetic energy of the barotropic forcing and the characteristic area of the obstacle cross-section, the integrated TKE is largest at the lowest $Ex = 0.066$ and is reduced by almost an order of magnitude at $Ex = 1$.

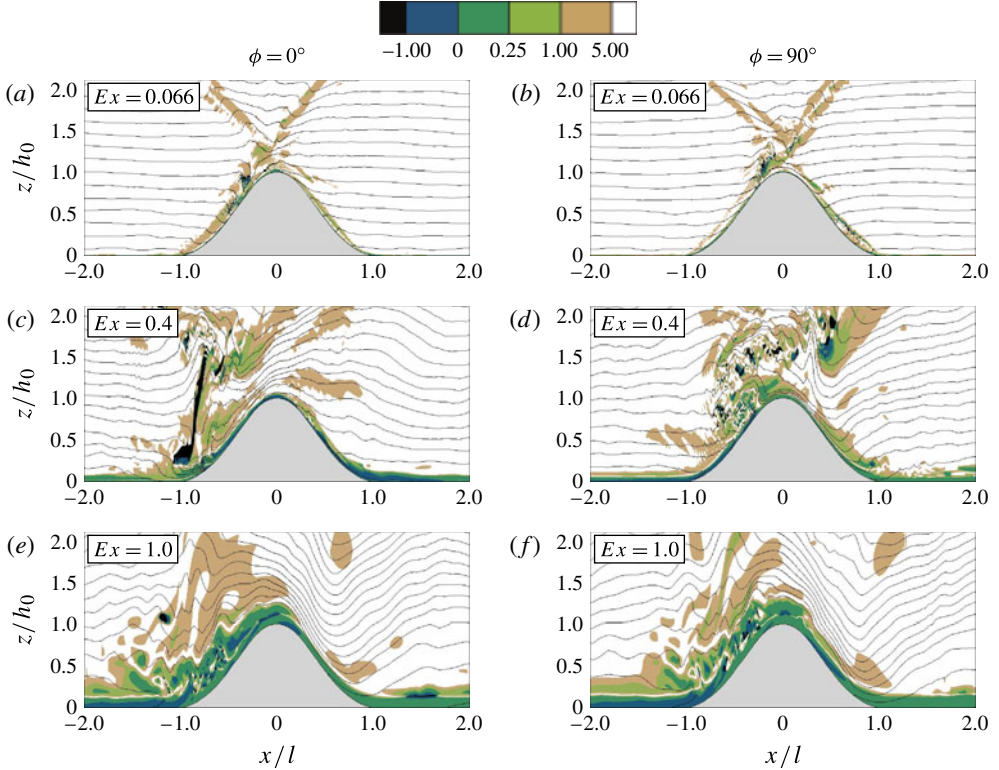


FIGURE 9. (Colour online) Plots of Ri_g and isopycnals near the topography for $Ex=0.066$, $Ex=0.4$ and $Ex=1$ are shown at $t/T=6.0$ (phase 0°) and $t/T=6.25$ (phase 90°).

At the lower excursion numbers, there is significant turbulence above the topography, i.e. TKE extends to almost two topographic heights above the flat bottom, $z=0$. The spatial organization of different terms in the cycle-averaged TKE balance is shown in figure 11. In all cases, shear production, P , is the primary overall source in the TKE balance. Integrated buoyancy flux is positive and a significant source of turbulence in the regions of convective instability: on and above the critical slope at $Ex=0.066$, and in the transient breaking lee waves at $Ex=0.04$ and $Ex=1.0$. Advection is an important component of the TKE balance since it spatially redistributes TKE from areas with significant shear or buoyancy production. For instance, at $Ex=0.04$, advection acts to redistribute energy from the region with wave breaking (a sink term in figure 11e) to the region near the crest (a source term in figure 11e). The spatial organization of the turbulent dissipation is similar to that of the turbulent production.

We now discuss temporal patterns of turbulence. A remarkable finding at $Ex=0.066$ is the temporal growth of turbulence (figure 12) in the radiated internal wave beam. Figure 12 shows the evolution of u_{rms}/U_0 at different points that belong to the internal wave beam (dashed line in figure 2a) and located by their normalized height above bottom z_b/h_0 . Higher locations in the beam exhibit turbulence at later time, e.g. even a location as high as $z_b/h_0=3$ exhibits TKE after six cycles. In addition to the advection of turbulence from the crest into the beam, the large shear within the beams leads to instability.

Field study of turbulence often involves interpretation of the time evolution of the flow at a few vertical moorings. The time evolution of the vertical profiles of

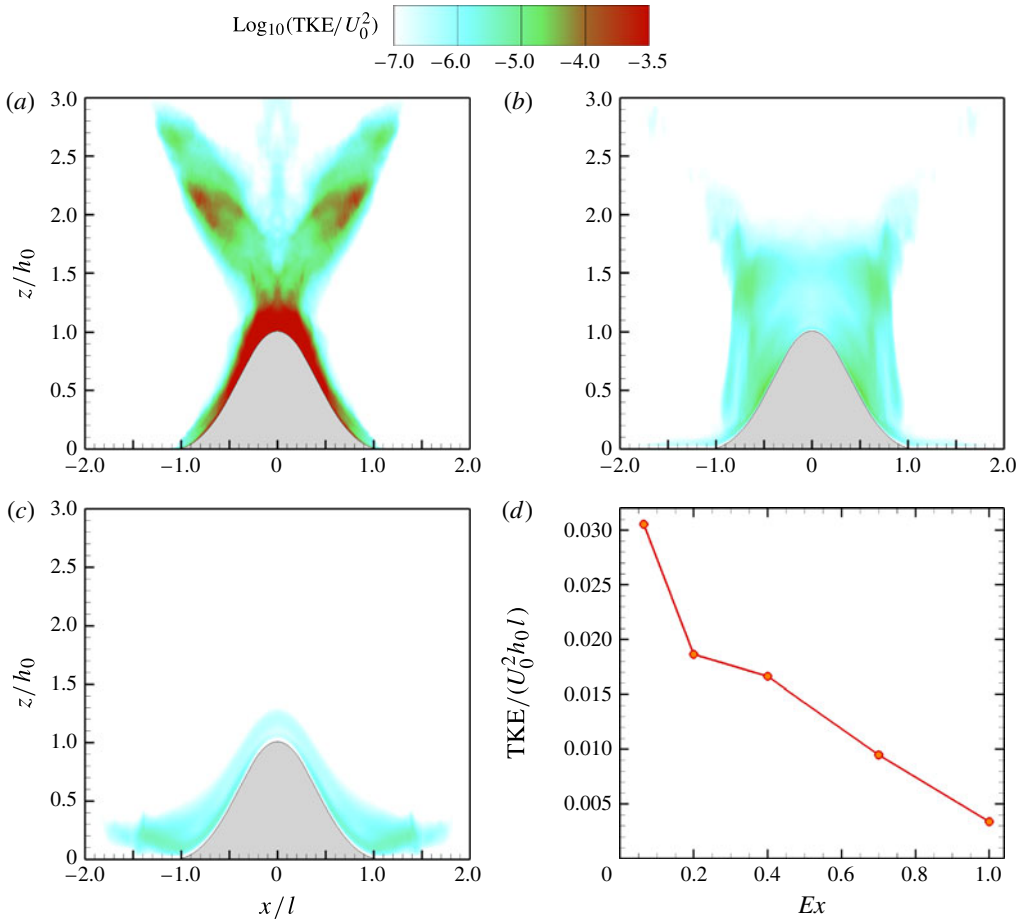


FIGURE 10. (Colour online) The spatial organization of cycle-averaged TKE normalized by U_0^2 : (a) $Ex = 0.066$, (b) $Ex = 0.4$ and (c) $Ex = 1.0$. Panel (d) shows the cycle-averaged TKE integrated between $-2 < x/l < 2$ and normalized with the barotropic TKE and characteristic obstacle area ($U_0^2 h_0 l$) as a function of Ex .

normalized TKE at the summit, $x/l = 0$, and at approximately midslope, $x/l = -0.4$, is shown in figure 13(a–f) over two tidal cycles. It is noteworthy that, when normalized by the barotropic forcing, the case with largest $Ex = 1.0$ has the weakest turbulence, in terms of both time duration and height from the bottom. Also, as shown previously by Rapaka *et al.* (2013), TKE at the summit of the ridge shows two maxima in a cycle corresponding to the passage of turbulence from each of the two internal wave beams generated at the ridge flanks, but shows only one maximum at midslope. At $Ex = 0.066$, turbulence is present over the ridge throughout the cycle. Figure 13(b) shows that there is a near-bottom region of turbulence that becomes thicker during flow reversal from down to up at $t/T = n$ (n integer) as well as a region of weaker turbulence that originates in the internal wave beam above the slope at $z/h_0 \sim 2$. At the summit (figure 13a), beams from both flanks cross and the TKE is more extensive vertically and in time. The case with $Ex = 0.4$ has substantial near-bottom turbulence at midslope (figure 13d). The off-bottom peak at $z/h_0 \sim 2$ corresponds to a TKE patch from the opposite ridge flank being swept downslope while during the

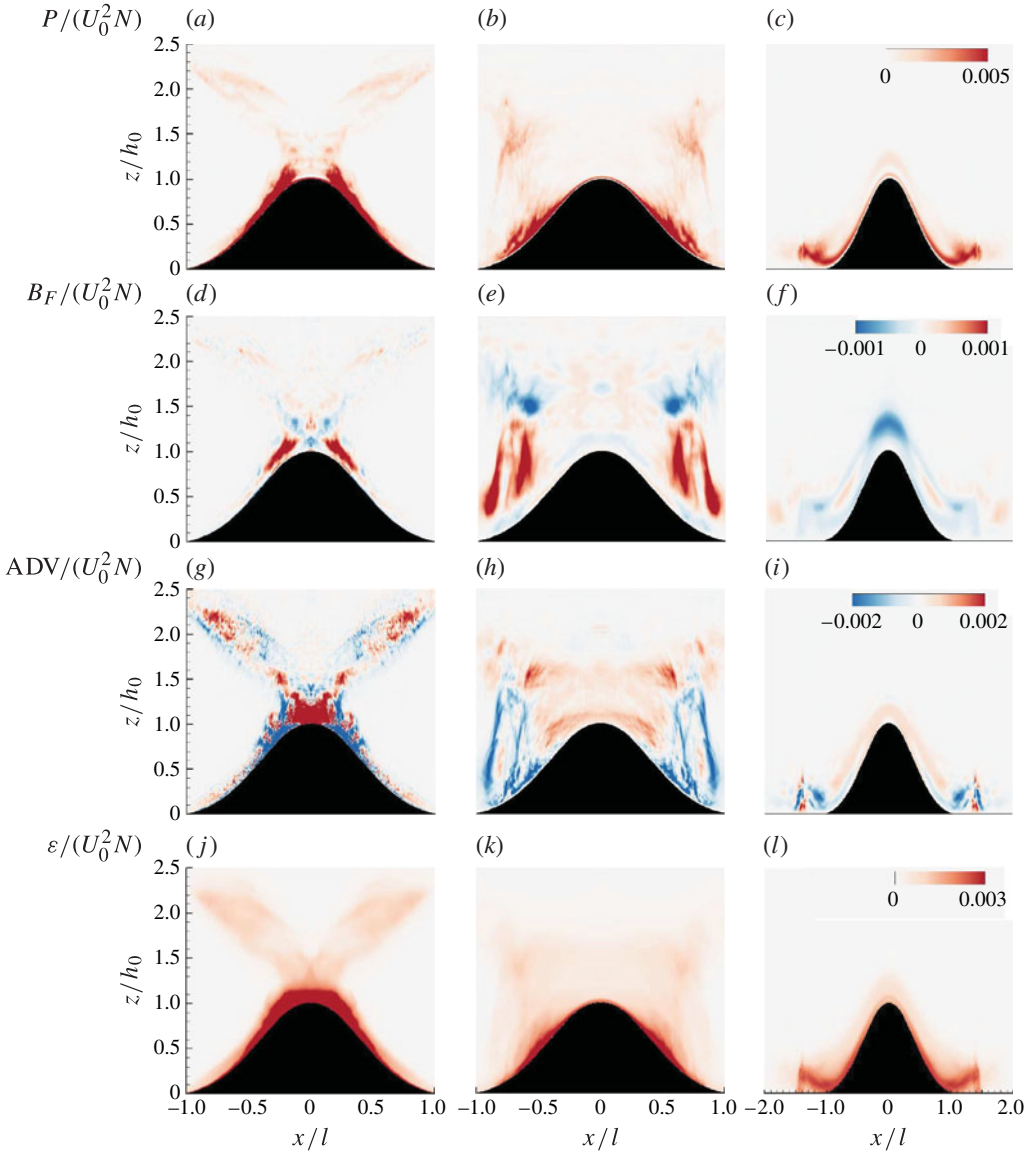


FIGURE 11. The spatial organization of cycle-averaged terms, normalized by $U_0^2 N$, in the TKE equation: (a–c) production; (d–f) buoyancy; (g–i) advection; and (j–l) dissipation. Panels (a,d,g,j), (b,e,h,k) and (c,f,i,l) correspond to $Ex = 0.066$, 0.4 and 1.0, respectively.

upslope phase there is an increase in TKE because of the upslope advection of the TKE patch that was initiated by the breaking lee wave. The case with $Ex = 1.0$ has strong turbulence when the barotropic velocity is large, either downslope or upslope.

6. Summary and conclusions

Three-dimensional DNS has been employed to investigate the effect of excursion number, Ex (the ratio of streamwise fluid advection length during a tidal cycle to streamwise topographic length scale), on the internal wavefield and turbulence at a

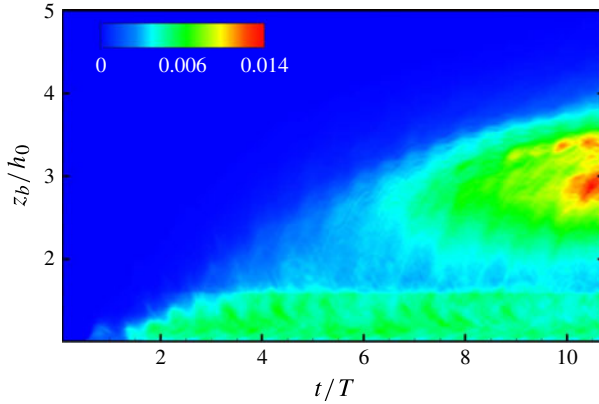


FIGURE 12. Temporal evolution of turbulence in the beam for case CEX1 ($Ex = 0.066$) with the normalized r.m.s. streamwise velocity, u_{rms} , used as the turbulence indicator. There are two beams as shown in figure 2, and u_{rms} at a particular z_b/h_0 is obtained by averaging over u_{rms} at points on the horizontal line $z = z_b$ that belong to either beam.

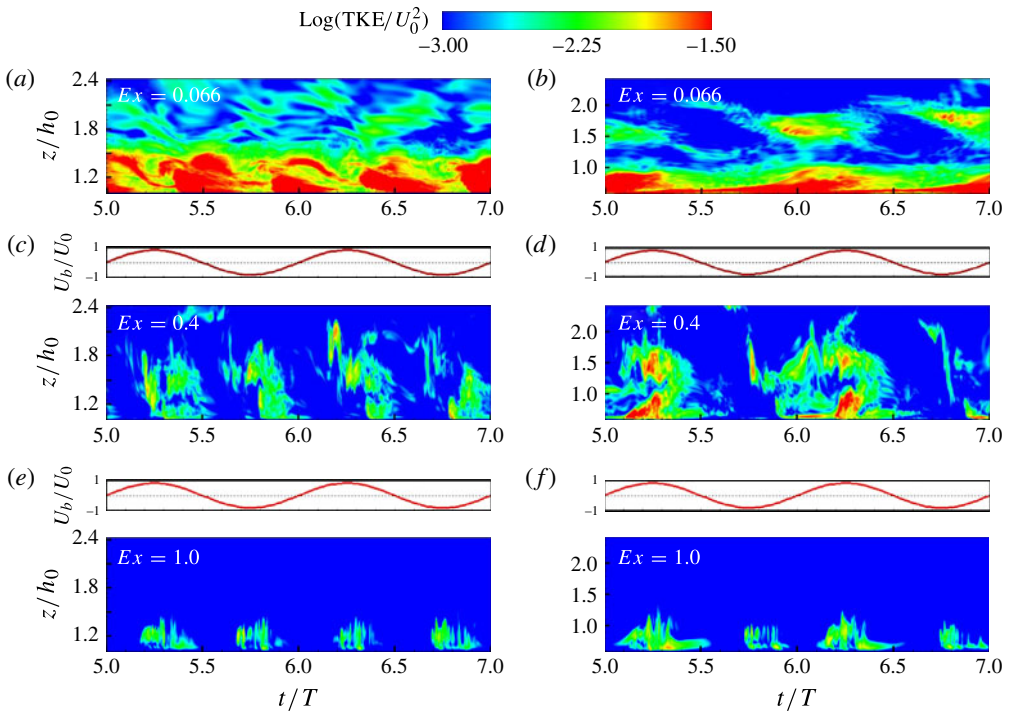


FIGURE 13. Temporal evolution of vertical profiles of $\log_{10}(\text{TKE}/U_0^2)$ at (a,c,e) the ridge summit and (b,d,f) the midslope of the left flank. Panels (a,b) correspond to $Ex = 0.066$, (c,d) to $Ex = 0.4$ and (e,f) to $Ex = 1.0$.

laboratory-scale obstacle with smoothed triangular topography. The excursion number Ex is increased from 0.066 to 1.0 while Re_s , the Reynolds number based on the Stokes boundary layer thickness, is kept constant. In the previous work of Rapaka

et al. (2013), the tidal forcing was systematically increased so that both Ex and Re_s increased and, moreover, the simulations were performed in the low- Ex regime. Here, we focus on the independent effect of Ex when Re_s is held constant and, furthermore, explore the $Ex = O(1)$ regime. The topography chosen is that with a constant slope portion (20% of slope length) inclined at the critical angle. The present simulations provide new results summarized below from which we infer that changing Ex from small to $O(1)$ values leads to qualitative changes in the wavefield as well as in the near-field turbulence.

With increasing Ex , the beam structure of the radiated wavefield becomes less evident, and the baroclinic intensification of velocity in both the boundary layer and the beams is reduced. The reason is that, when tidal excursion length increases, the fluid particle nominally on the critical slope is advected on to subcritical regions, attenuating the resonant wave response. In the present simulations with $Ex = 0.4$ and larger, visualizations show the presence of transient lee waves. At $Ex = 1$, lee wave phase lines can be clearly identified at birth and have inclination in close agreement with linear theory of steady lee waves. Evaluation of the cycle-averaged barotropic energy budget shows a reduction of approximately 25% in the radiated wave flux at $Ex = 1$, which is attributed to increased baroclinic dissipation and the advective flux as well as reduction of conversion. The numerically computed value of the linear approximation of conversion using boundary values remains almost invariant with respect to Ex . Interestingly, the hydrostatic component of the linear conversion increases when Ex exceeds 0.4 (when transient lee waves are identified), but this increase is compensated by a reduction in the non-hydrostatic component. The spatial distribution of cycle-averaged terms in the baroclinic energy budget is examined. The radiative flux, which is concentrated along the beams at low Ex , becomes less localized at high Ex . The baroclinic dissipation occurs in the beams at low Ex , unlike the situation at high Ex , where the baroclinic dissipation is much larger in the boundary layer.

Turbulence changes qualitatively among the cases with $Ex = 0.066$, 0.4 and 1.0. The $Ex = 0.066$ case has turbulence in the radiated beams. Advection of turbulent patches from the slope and intensified velocity shear lead to beam instability, which eventually becomes strong enough to generate turbulence in the radiated beam. TKE production (mainly by shear and to a lesser extent by buoyancy) is strongest at and above the critical slope, and advection distributes TKE from the slope to the crest. It is worth noting that, although cycle-averaged TKE production by buoyancy is small, it is the convective instability during flow reversal from down- to upslope flow (Gayen & Sarkar 2011a) that causes transition to turbulence over the entire height of the local boundary layer. The case with $Ex = 0.4$ has the tallest turbulent overturns, up to two obstacle heights from the flat bottom. The source in the TKE balance is TKE production, concentrated near the lower flanks, as well as the buoyancy, concentrated in the tall overturning regions adjacent to the topography that have vertical strain and gravitational instability. The overturns are initiated during flow reversal from downslope to upslope in the transient lee waves akin to the finding of Legg & Klymak (2008), although the nonlinearity in flow response has different origins: Ex based on the streamwise length of the small obstacle considered here is $O(1)$, while Legg & Klymak (2008) consider large obstacles with low value of Ex but strongly supercritical slope, leading to $O(1)$ values of Ex_{in} , based on a dynamically determined inner streamwise length scale (Winters & Armi 2013), that is applicable near the crest. In the present simulation with $Ex = 1.0$, internal wave beams are nearly absent, the shear and strain in the upper water column is weak and, therefore,

turbulence is limited to a near-bottom layer over the obstacle and adjoining flat bottom. The spatial organization of gradient Richardson number, Ri_g , shows close relationship to the TKE patches, indicating convective and shear instabilities in the corresponding regions. The temporal evolution and phase dependence of vertical profiles of density, velocity and turbulence are also investigated and show differences between the slope and the crest, as can be anticipated from the preceding discussion.

We conclude that small-scale topographies with energetic tides, corresponding to the regime of $Ex = O(1)$, are not as efficient radiators of internal wave energy as topographies with small Ex . The dependence of the local loss, q , of baroclinic energy is obtained without recourse to parametrization or artificially large numerical diffusivity in the present DNS study, but the robustness of this result to larger, more realistic, length scales needs to be established. Furthermore, the influence of Ex in situations with supercritical topography needs examination through turbulence-resolving simulations.

Acknowledgements

We are grateful for the support of ONR grant N00014-09-1028 (program manager Dr T. Paluszkiwicz).

REFERENCES

- AFANASYEV, Y. D. & PELTIER, W. R. 1998 The three-dimensionalisation of stratified flow over two-dimensional topography. *J. Atmos. Sci.* **55**, 19–39.
- ALFORD, M. H., MACKINNON, J. A., NASH, J. D., SIMMONS, H., PICKERING, A., KLYMAK, J. M., PINKEL, R., SUN, O., RAINVILLE, L., MUSGRAVE, R., BEITZEL, T., FU, K. & LU, C. 2011 Energy flux and dissipation in Luzon Strait: two tales of two ridges. *J. Phys. Oceanogr.* **41**, 2211–2222.
- AUCAN, J. & MERRIFIELD, M. A. 2008 Boundary mixing associated with tidal and near-inertial internal waves. *J. Phys. Oceanogr.* **38**, 1238–1252.
- AUCAN, J., MERRIFIELD, M. A., LUTHER, D. S. & FLAMENT, P. 2006 Tidal mixing events on the deep flanks of Kaena Ridge, Hawaii. *J. Phys. Oceanogr.* **36**, 1202–1219.
- BAINES, P. G. 1995 *Topographic Effects in Stratified Flows*. Cambridge University Press.
- BALMFORTH, N. J., IERLEY, G. R. & YOUNG, W. R. 2002 Tidal conversion by subcritical topography. *J. Phys. Oceanogr.* **32**, 2900–2914.
- BELL, T. H. 1975a Lee waves in stratified fluid with simple harmonic time dependence. *J. Fluid Mech.* **67**, 705–722.
- BLUTEAU, C. E., JONES, N. L. & IVEY, G. N. 2011 Dynamics of a tidally forced stratified shear flow on the continental slope. *J. Geophys. Res.* **116**, C11017.
- CACCHIONE, D. A., PRATSON, L. F. & OGSTON, A. S. 2002 The shaping of continental slopes by internal tides. *Science* **296**, 724–727.
- CARTER, G. S. & GREGG, M. C. 2002 Intense, variable mixing near the head of Monterey Submarine Canyon. *J. Phys. Oceanogr.* **32**, 3145–3165.
- CARTER, G. S., MERRIFIELD, M. A., BECKER, J. M., KATSUMATA, K., GREGG, M. C., LUTHER, D. S., LEVINE, M. D., BOYD, T. J. & FIRING, Y. L. 2008 Energetics of m_2 barotropic-to-baroclinic tidal conversion at the Hawaiian Islands. *J. Phys. Oceanogr.* **38**, 2205–2223.
- ECHEVERRI, P. & PEACOCK, T. 2010 Internal tide generation by arbitrary two-dimensional topography. *J. Fluid Mech.* **659**, 247–266.
- GARRETT, C. & KUNZE, E. 2007 Internal tide generation in the deep ocean. *Annu. Rev. Fluid Mech.* **39**, 57–87.
- GAYEN, B. & SARKAR, S. 2010 Turbulence during the generation of internal tide on a critical slope. *Phys. Rev. Lett.* **104**, 218502.

- GAYEN, B. & SARKAR, S. 2011a Boundary mixing by density overturns in an internal tidal beam. *Geophys. Res. Lett.* **38**, L14608.
- GAYEN, B. & SARKAR, S. 2011b Direct and large eddy simulations of internal tide generation at a near critical slope. *J. Fluid Mech.* **681**, 48–79.
- GOSTIAUX, L. & DAUXOIS, T. 2007 Laboratory experiments on the generation of internal tidal beams over steep slopes. *Phys. Fluids* **19**, 028102.
- KANG, D. & FRINGER, O. 2012 Energetics of barotropic and baroclinic tides in the Monterey Bay area. *J. Phys. Oceanogr.* **42**, 272–290.
- KLYMAK, J. M., MOUM, J. N., NASH, J. D., KUNZE, E., GIRTON, J. B., CARTER, G. S., LEE, C. M., SANFORD, T. B. & GREGG, M. C. 2006 An estimate of tidal energy lost to turbulence at the Hawaiian ridge. *J. Phys. Oceanogr.* **36**, 1148–1164.
- KLYMAK, J. M., PINKEL, R. & RAINVILLE, L. 2008 Direct breaking of the internal tide near topography: Kaena ridge, Hawaii. *J. Phys. Oceanogr.* **38**, 380–399.
- KUNZE, E. & TOOLE, J. M. 1997 Tidally driven vorticity, diurnal shear and turbulence atop Fieberling Seamount. *J. Phys. Oceanogr.* **27**, 2663–2693.
- LEDWELL, J. R., MONTGOMERY, E. T., POLZIN, K. L., ST LAURENT, L. C., SCHMITT, R. W. & TOOLE, J. M. 2000 Evidence for enhanced mixing over rough topography in the abyssal ocean. *Nature* **403**, 179–182.
- LEGG, S. & HUIJTS, K. M. H. 2006 Preliminary simulations of internal waves and mixing generated by finite amplitude tidal flow over isolated topography. *Deep-Sea Res. II* **53**, 140–156.
- LEGG, S. & KLYMAK, J. 2008 Internal hydraulic jumps and overturning generated by tidal flows over a tall steep ridge. *J. Phys. Oceanogr.* **38**, 1949–1964.
- LEVINE, M. D. & BOYD, T. J. 2006 Tidally forced internal waves and overturns observed on a slope: results from HOME. *J. Phys. Oceanogr.* **36**, 1184–1201.
- LIM, K., IVEY, G. N. & JONES, N. L. 2010 Experiments on the generation of internal waves over continental shelf topography. *J. Fluid Mech.* **663**, 385–400.
- LLEWELLYN SMITH, S. G. & YOUNG, W. R. 2002 Conversion of the barotropic tide. *J. Phys. Oceanogr.* **32**, 1554–1566.
- LUECK, R. G. & MUDGE, T. D. 1997 Topographically induced mixing around a shallow seamount. *Science* **276**, 1831–1833.
- MOUM, J. N., CALDWELL, D. R., NASH, J. D. & GUNDERSON, G. D. 2002 Observations of boundary mixing over the continental slope. *J. Phys. Oceanogr.* **32**, 2113–2130.
- MUNK, W. & WUNSCH, C. 1998 Abyssal recipes II: energetics of tidal and wind mixing. *Deep-Sea Res. I* **45**, 1977–2010.
- NASH, J. D., ALFORD, M. H., KUNZE, E., MARTINI, K. & KELLY, S. 2007 Hotspots of deep ocean mixing on the Oregon continental slope. *Geophys. Res. Lett.* **34**, L01605.
- PÉTRÉLIS, F., LLEWELLYN SMITH, S. G. & YOUNG, W. R. 2006 Tidal conversion at submarine ridge. *J. Phys. Oceanogr.* **36**, 1053–1071.
- POLZIN, K., OAKEY, N. S., TOOLE, J. M. & SCHMITT, R. W. 1996 Fine structure and microstructure characteristics across the north west Atlantic subtropical front. *J. Geophys. Res.* **101**, 14111–14121.
- POLZIN, K. L., TOOLE, J. M., LEDWELL, J. R. & SCHMITT, R. W. 1997 Spatial variability of turbulent mixing in the abyssal ocean. *Science* **276**, 93–96.
- RAPAKA, N. R., GAYEN, B. & SARKAR, S. 2013 Tidal conversion and turbulence at a model ridge: direct and large eddy simulation. *J. Fluid Mech.* **715**, 181–209.
- RUDNICK, D. L., BOYD, T. J., BRAINARD, R. E., CARTER, G. S., EGBERT, G. D., GREGG, M. C., HOLLOWAY, P. E., KLYMAK, J. M., KUNZE, E., LEE, C. M., LEVINE, M. D., LUTHER, D. S., MARTIN, J. P., MERRIFIELD, M. A., MOUM, J. N., NASH, J. D., PINKEL, R., RAINVILLE, L. & SANFORD, T. B. 2003 From tides to mixing along the Hawaiian Ridge. *Science* **301**, 355–357.
- SAENKO, O. A. & MERRYFIELD, W. J. 2005 On the effect of topographically enhanced mixing on the global ocean circulation. *J. Phys. Oceanogr.* **35**, 826–834.
- SIMMONS, H. L., JAYNE, S. R., ST LAURENT, L. C. & WEAVER, A. J. 2004 Tidally driven mixing in a numerical model of the ocean general circulation. *Ocean Model.* **6**, 245–263.

- ST LAURENT, L. C., STRINGER, S., GARRETT, C. & PERRAULT-JONCAS, D. 2003 The generation of internal tides at abrupt topography. *Deep-Sea Res. I* **50**, 987–1003.
- ST LAURENT, L. C., TOOLE, J. M. & SCHMITT, R. W. 2001 Buoyancy forcing by turbulence above rough topography in the abyssal Brazil Basin. *J. Phys. Oceanogr.* **31**, 3476–3495.
- WAIN, D. J., GREGG, M. C., ALFORD, M. H., LIEN, R.-C., HALL, R. A. & CARTER, G. S. 2013 Propagation and dissipation of the internal tide in upper Monterey Canyon. *J. Geophys. Res.* **118**, 1–23.
- WINTERS, K. B. & ARMI, L. 2013 The response of a continuously stratified fluid to an oscillating flow past an obstacle. *J. Fluid Mech.* **727**, 83–118.
- YAKOVENKO, S. N., THOMAS, T. G. & CASTRO, I. P. 2011 A turbulent patch arising from a breaking internal wave. *J. Fluid Mech.* **677**, 103–133.
- ZHANG, H. P., KING, B. & SWINNEY, H. L. 2008 Resonant generation of internal waves on a model continental slope. *Phys. Rev. Lett.* **100**, 244504.